# Effect of Surface Roughness and Chemical Composition of Metastable Austenitic Stainless Steels on Electrochemical Polishing-Induced Martensitic Transformation

JUNYOUNG CHAE, HOJUN GWON, CHANWOO JEONG, HYUKJAE LEE, GUIHYUNG LEE, HYUNGJUN CHO, SUNG-JOON KIM, and HEUNG NAM HAN

Herein, we analyzed the martensitic transformation kinetics during electrochemical polishing (EP) for stainless steel specimens with varying surface roughness and austenite stability. Martensite fraction measurement demonstrated that specimens with higher surface roughness and lower austenite stability exhibited relatively higher levels of martensitic transformation. To understand these phase transformation characteristics, the amount of charge build-up on the specimen surface during EP was calculated using COMSOL Multiphysics simulations for specimens with different surface roughness. The effect of charge build-up-induced stress was analyzed using previously published first-principles calculations. We found that specimens with higher surface roughness accumulated more charge build-up, resulting in greater stress and a martensitic transformation driving force. Furthermore, the critical energy required for the martensitic transformation was calculated using Thermo-Calc for specimens with different austenite stabilities. We demonstrated that the martensitic transformation kinetics during EP could be explained in terms of austenite stability, similar to the stress-induced martensitic transformation.
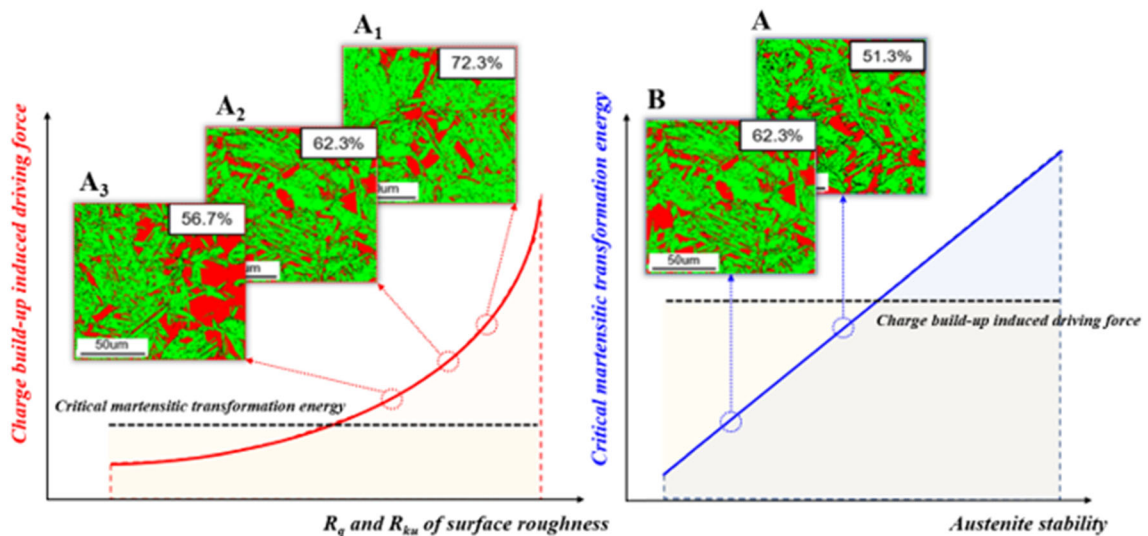
© The Author(s) 2024

JUNYOUNG CHAE, CHANWOO JEONG, HYUKJAE LEE, GUIHYUNG LEE, and HEUNG NAM HAN are with the Department of Materials Science and Engineering & Research Institute of Advanced Materials, Seoul National University, Seoul 08826, Republic of Korea. Contact e-mail: hnhan@snu.ac.kr HOJUN GWON, HYUNGJUN CHO, and SUNG-JOON KIM are with the Graduate Institute of Ferrous Technology, Pohang University of Science and Technology, Pohang 37673, Republic of Korea.

I. INTRODUCTION

THE electroplasticity effect is a phenomenon in which the application of an electric current to a material decreases flow stress and increases ductility without significantly increasing temperature owing to Joule heating. Troitskii[1] first observed a phenomenon in which flow

stress decreased when an electric current was applied during tension and compression experiments using various metallic materials. Conrad[2,3] conducted research on the application of current during plastic deformation and reported that the basis of the electroplasticity effect is not limited to the Joule heating effect. Several researchers have analyzed the mechanical behavior of aluminum, copper, and brass alloys under the application of an electric current[4–6] and have captured the existence of an athermal effect, which is distinct from the Joule heating effect. In addition, studies investigating the effects of electric current on the microstructural changes in metallic materials, such as annealing,[7–9] aging,[10–12] dissolution,[13,14] recrystallization,[15] and healing,[16,17] have reported that the athermal effect accompanying the Joule heating effect during electric current treatment enhances the kinetics of the material compared to a control group where only the Joule heating effect is present. In a study aimed at elucidating the mechanism of kinetic enhancement by the athermal effect,[18] the authors focused on the charge build-up/charge imbalance phenomenon that occurs near defects during current applications using first-principles calculations, microstructure-based finite element analysis, and experimental approaches. It was proposed that charge build-up/charge imbalance changes the shape of the interatomic potential, triggering variations in the bond energy and equilibrium atomic spacing, which constitute the main mechanism underlying the athermal effect.

Electrochemical polishing (EP) is a surface treatment method that utilizes an electrochemical reaction resulting in the dissolution of metals from the surface as metal ions. Unlike surface treatment methods that apply direct stress or deformation to the surface (i.e., mechanical polishing[19] or focused ion beam milling[20]), EP treatment is a noncontact polishing method between the electrode and the workpiece. Recently, a phenomenon in which austenite in metastable stainless steel transforms into martensite during the anodic charging of EP treatment was observed.[21] The authors attributed this phenomenon to the changes in the shape of the interatomic potential owing to charge build-up, similar to the athermal effect. The EP treatment accumulates electric charges on the surface of the specimen simultaneously with the leaching of metal ions [Figure 1(a)]. The charge build-up during EP treatment generates a charge-imbalanced environment, and the resulting change in the shape of the interatomic potential leads to a variation in the equilibrium atomic spacing, which can induce a stress-induced martensitic transformation [Figure 1(b)]. As an extension of previous studies, this study analyzed the martensitic transformation occurring during the EP treatment of various stainless steel specimens with different surface roughness and austenite stabilities. The results demonstrated that the kinetics of martensitic transformation during the EP treatment also follow the same context as the stress-induced martensitic transformation.

II. MATERIALS AND EXPERIMENTAL DETAILS

Specimens A and B used in this study had different austenite stabilities owing to differences in their alloy element contents, and their chemical compositions are listed in Table I. An overview of the experimental preparation steps for specimens A and B is presented in Figure 2. To obtain different surface roughness values for each specimen, the specimens were subjected to a primary-EP treatment using a 10 pct perchloric acid-90 pct acetic acid mixture as the electrolyte under a voltage of 20 V for 60, 120, and 180 seconds. To prevent oxidation during heat treatment, the primary-EP treated specimens were sealed in quartz tubes under a vacuum and then annealed at 1100 °C for 1 hour to obtain 100 pct austenite phase, followed by water quenching. Subsequently, a secondary-EP treatment was performed using the same electrolyte as that in the primary-EP treatment step for 30, 60, 120, and 180 seconds. Meanwhile, the specimens were set as the anode to avoid martensite formation owing to hydrogen charging during the secondary-EP treatment.[22] And the martensite fraction was obtained at each time step using electron backscatter diffraction system (Gemini 560 SEM; ZEISS) under conditions of an acceleration voltage of 15 kV and a step size of 0.4 μm to observe the martensitic transformation occurring during electropolishing. In addition, further microstructural information on grain size and dislocation density for prepared specimens A and B has been included in the Supplementary material (see Figures S-1, S-2, and S-3). Meanwhile, we have documented the negligible temperature changes resulting from the heat generated by the electrical current input during the secondary-EP treatment process also in the Supplementary material (see Figures S-4 and S-5). Based on this information, we intend to proceed with the analysis, disregarding the effects of heat generation due to the electrical current application.

Because an electrochemical reaction occurs at the surface of the specimen during EP treatment, it is closely related to the surface morphology. Therefore, a 3D image of the specimen surface was obtained before the secondary-EP treatment through atomic force microscopy (NX-10; Park Systems). Furthermore, we statistically analyzed the surface asperities using surface roughness parameters, such as the root mean square deviation (R_q) and kurtosis (R_{ku}). The formulas for R_q and R_{ku} are given below.[23,24]

$$R_q = \sqrt{\frac{1}{l}\int_0^l Z^2(x)\mathrm{d}x} \qquad [1]$$

$$R_{ku} = \frac{1}{R_q^4}\left[\frac{1}{l}\int_0^l Z^4(x)\mathrm{d}x\right], \qquad [2]$$

where l and x represent the base length and absolute horizontal coordinate, respectively, and Z(x) represents the absolute vertical coordinate. We defined the R_q and R_{ku} values before the primary-EP and heat treatment as the initial surface roughness and investigated the effect of changes in the initial surface roughness on the martensitic transformation.
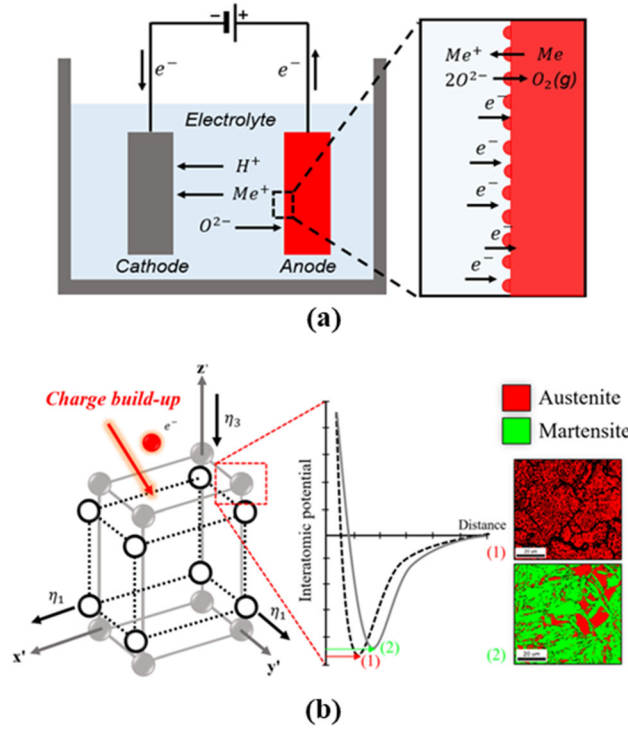
(a)

(b)

Fig. 1—(a) Schematic diagram of EP and oxidation-reduction reactions occurring around the surface asperity of the metallic specimen, and (b) Mechanism of martensitic transformation induced by charge build-up during EP treatment.

Table I. Chemical Composition (Weight Percent) of Two Alloys A and B

	Element							
Alloy	C	N	Si	Mn	Cr	Ni	Mo	Fe
A	0.15	0.1	0.9	0.3	16	5	0.7	bal.
B	0.08	0.1	0.9	0.3	15.9	6.1	0.7	bal.

III. FINITE ELEMENT MODEL FOR ELECTROCHEMICAL POLISHING

To analyze the kinetics of the martensitic transformation occurring during the EP treatment, a COMSOL Multiphysics simulation model[25] was constructed to calculate the electrochemical etching kinetics and the amount of charge build-up on the stainless steel surface during the EP treatment. During EP treatment, a preferential anodic reaction occurs on the surface asperities of the specimen resulting in the elution of metal ions and the charge build-up.[26] A COMSOL Multiphysics simulation was constructed to calculate the amount of charge build-up that accumulated at the asperities during the aforementioned chemical reaction, as depicted in Figure 3.

The specimen surface, including the asperities, was modeled as a 2D columnar structure with dimensions of $100 \times 20 \ \mu m^2$ in contact with a 90 pct acetic acid-10 pct perchloric acid electrolyte. The asperity shape was based on surface roughness data measured using AFM, with heights of 104.5, 77.9, and 50.3 nm, and sharpness values of 2.21, 2.15, and 2.11 for A_1, A_2, and A_3, respectively, determined from root mean square deviation (R_q) and kurtosis (R_{ku}) of the surface roughness data. The simulations were conducted with the lower boundary fixed at ground potential, the upper boundary at 20 V, and the left and right boundaries insulated to avoid potential boundary effects. The authors referred to our previous studies[21] to formulate the constitutive equation, and added the following equation to realistically simulate the electrochemical reaction.

The Nernst–Planck equation is used to describe the movement of ions through electro-diffusion in relation to their concentration[27]:

$$N_i = -z_i \mu_i F C_i \nabla \Phi - D_i \nabla C_i + C_i v, \quad [3]$$

where the symbols $N_i, z_i, \mu_i, C_i, D_i$ represent the flux density, charge, mobility, concentration, and diffusivity for species i. Meanwhile, and $F, \nabla \Phi, \nabla C_i, v$ is a Faraday's constant, electric field, concentration gradient, and velocity vector, respectively. If there are no homogeneous reactions happening within the electrolyte, then the material balance can be determined by following equation:

$$\frac{\partial C_i}{\partial t} + \nabla \cdot N_i = 0, \quad [4]$$

where t is time. The migration of ions was modeled by linking mobility to diffusion *via* the Nernst-Einstein relation:

$$u_i = \frac{z_i F D_i}{RT} \quad [5]$$

The reaction kinetics including rate of an electrochemical reaction and the current density flowing through an electrode is given by the Butler-Volmer equation[27]:

$$i_{BV} = i_0 \left(\exp\left(\frac{(1-\alpha)F\eta}{RT}\right) - \exp\left(\frac{-\alpha F\eta}{RT}\right) \right), \quad [6]$$

where i_0, α, η stands for the equilibrium corrosion current density, charge transfer coefficient and overpotential, respectively. The overpotential η is defined as

$$\eta = \Phi_s - \Phi_l, \quad [7]$$

where Φ_s, Φ_l are the potential of the solid electrode and the electrolyte adjacent to the electrode, respectively. Table II shows the material parameters for EP simulation used in the above constitutive equations.

IV. RESULTS AND DISCUSSION

A. *Identification of the Specimen Surface Morphology Using Atomic Force Microscopy*

Figure 4 shows that a large number of uneven asperities are distributed on the surface of specimen A. We quantitatively identified the morphological
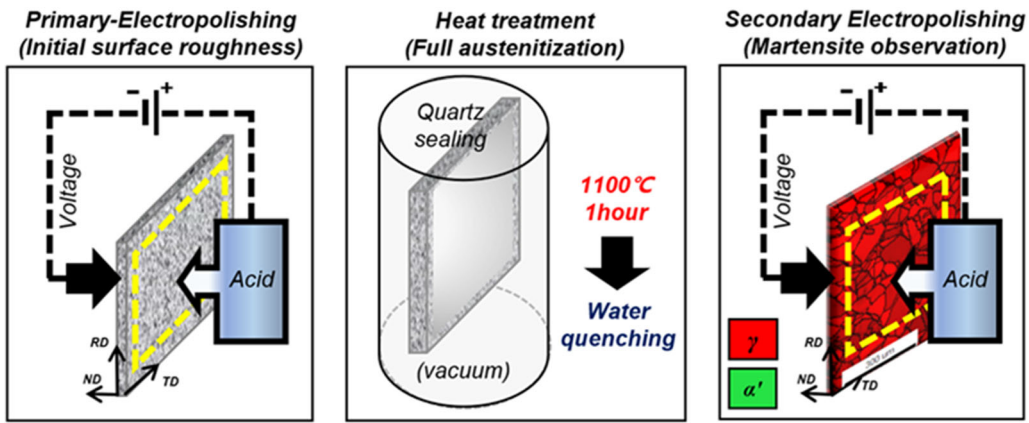
Fig. 2—Experimental scheme: Primary-EP treatment for removing surface oxide and controlling initial surface roughness, Heat treatment performed in a quartz tube to make 100 pct austenite microstructure followed by water quenching, and Secondary-EP treatment conducted to observe the effect of EP treatment on the martensitic transformation.
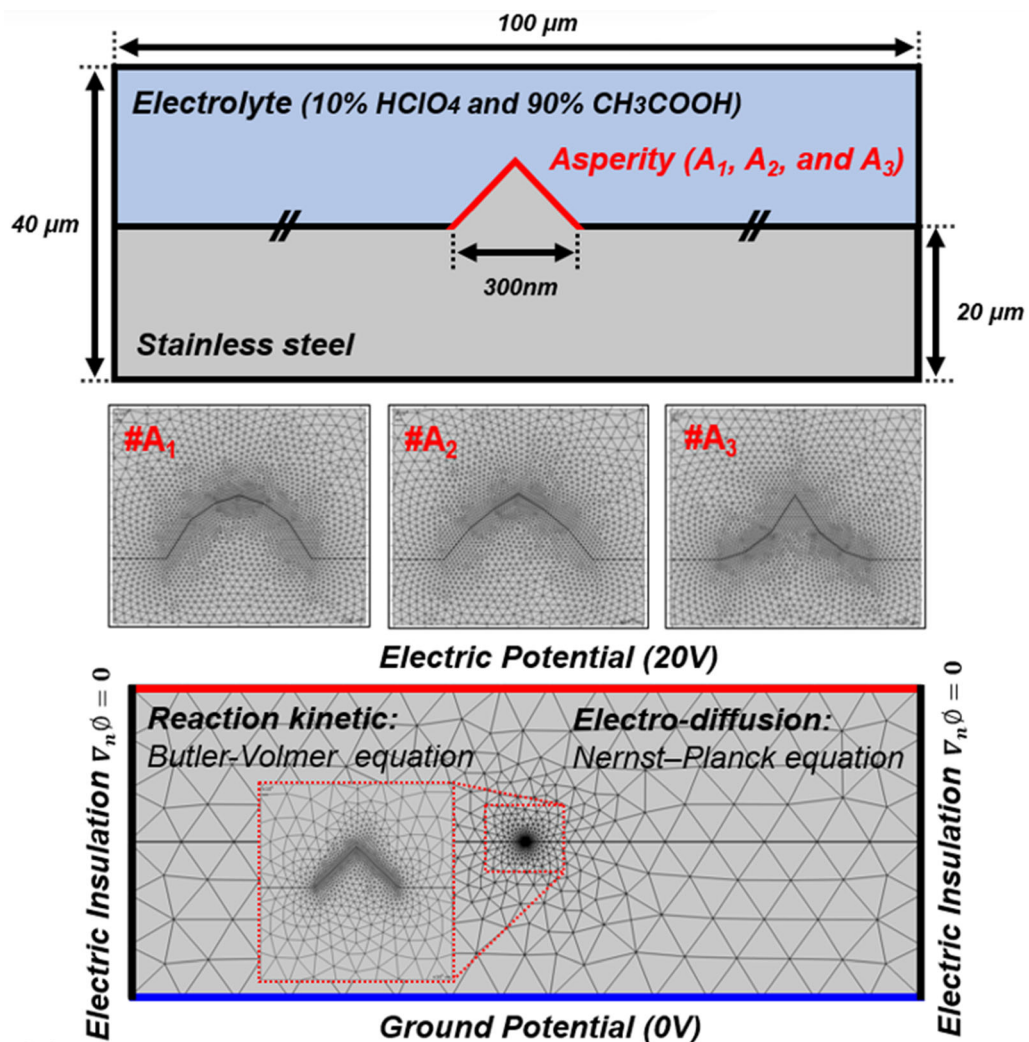

Fig. 3—Overview of the EP simulation model: designed simulation conditions and dimensions for EP, and differently defined asperities and their corresponding mesh conditions (A_1, A_2, and A_3) and boundary conditions for EP simulation.

characteristics of asperities statistically using surface roughness parameters.

The surface roughness parameters R_q and R_{ku} of steel specimens A and B were measured at primary-EP durations of 60, 120, and 180 seconds, as shown in Figure 5. The average R_q values for the A steel when primary-EP was performed for 60, 120, and 180 seconds were 104.5, 77.9, and 50.3 nm, and the average R_{ku} values were 2.21, 2.15, and 2.11, respectively. For B steel, the average R_q values when primary-EP was performed for 60, 120, and 180 seconds were 82.2, 56.1, and 40.9 nm, and the average R_{ku} values were 2.16, 2.08, and 2.01, respectively. As the primary-EP duration increased, the R_q and R_{ku} values decreased for both specimens A and B, indicating that the initial surface roughness of the specimen before the secondary-EP step can be controlled by adjusting the duration of the primary-EP step; as the primary-EP duration increased, the specimen tended to have asperities with a lower (low R_q) and duller (low R_{ku}) shape.

B. *Observation of Martensitic Transformation of the Specimens with Different Initial Surface Roughness and Austenite Stability During Secondary-EP*

Figure 6(a) shows the phase maps obtained by EBSD for specimens A and B after the secondary-EP treatment for 30, 60, 120, and 180 seconds. Before the secondary-EP treatment, all specimens were confirmed to have a 100 pct austenite phase, indicating the primary-EP and heat treatment worked well. Meanwhile, specimens A and B treated with secondary-EP exhibited a rapid increase in the martensite phase fraction with duration, followed by a tendency to converge to a certain phase fraction. Herein, the specimens were named according to the duration of the primary-EP treatment that affects the initial surface roughness for convenience when comparing the specimens with various initial surface roughness and austenitic stability: The A specimens were further labeled as A_1, A_2, and A_3, corresponding to the duration of the primary-EP treatment for 60, 120, and 180 seconds, respectively; B specimens were labeled as B_1 corresponding to the duration of the primary-EP treatment for 60 seconds.

C. *EP-Induced Martensitic Transformation Analyzed in Terms of the Amount of Charge Imbalance in Specimens with Different Initial Surface Roughness*

To investigate the effect of the initial surface roughness on martensitic transformation, the martensite fractions of specimen A with different primary-EP durations are presented in Figure 6(b). After 30 seconds of the secondary-EP treatment, the martensite fractions of specimens A_1, A_2, and A_3 were 26.9, 24.9, and 13.0 pct, respectively. Notably, even with increased secondary-EP durations of up to 60, 120, and 180 seconds, the martensite fractions remained higher in the order of A_1, A_2, and A_3, indicating that specimens with high R_q and R_{ku} values (A_1) have a higher fraction of the martensite phase. Stress-induced martensitic transformation during EP treatment occurs because of charge

build-up on the surface asperities through electrochemical reactions.[21] The charge build-up occurs due to the presence of asperities on the specimen's free surface, clearly establishing a correlation between the two. To investigate the effect of the morphological characteristics on the amount of charge build-up, EP simulation was performed using COMSOL Multiphysics (see Supplementary Figure S-6).

As shown in Figure 7, the amount of the charge build-up per unit area (C/m^2) is shown for specimens A_1, A_2, and A_3. The maximum charge build-up occurs at the tip of the specimen asperity, with values of 3.02×10^{-3}, 2.79×10^{-3}, and 2.55×10^{-3} C/m^2 for specimens A_1, A_2, and A_3, respectively. The amount of charge build-up decreased as the initial surface roughness decreased due to etching. These results indicate that lower and blunt asperities lead to less amount of charge build-up. Figure 8(a) shows the outcomes of the first-principles calculations conducted in a previous study on the impact of charge build-up on stress development in the Fe lattice.[21] Charge build-up causes alterations in the interatomic potential shape, which changes the bonding energy and equilibrium atomic spacing, leading to stresses ranging from several hundred to several thousand megapascals. We calculated through EP simulation that different levels of the amount of charge build-up can be developed at the tip of asperity depending on the initial surface roughness. The stresses produced by the calculated charge build-up for specimens A_1, A_2, and A_3 were 472, 436, and 398 MPa, respectively. Under stress, we calculated the interaction energy, which is the driving force for martensitic transformation, to check whether the stress generated by charge build-up is sufficient to cause martensitic transformation as shown in Figure 8(b). The interaction energy accompanying lattice deformation during martensitic transformation can be obtained by calculating the transformation strain,[30,31] and the detailed calculation process was included in the previous work.[21] The interaction energies for specimens A_1, A_2, and A_3 were 367, 339, and 306 J/mol, respectively, indicating that the driving force for the martensitic transformation induced by the charge build-up was sequentially larger in the order of A_1, A_2, and A_3. This finding is consistent with the trend observed in the martensite fraction measured by EBSD, which increased in the order A_1, A_2, and A_3 [Figure 6(b)].

D. *Thermodynamic Analysis of EP-Induced Martensitic Transformation in Specimens of Different Austenitic Stability*

To compare the martensitic transformation behaviors of specimens A and B with different austenite stabilities, the initial surface roughness was set as the control variable. Because specimens A and B had different etching kinetics, the martensite fractions of the two specimens were compared after treating each specimen with a different primary-EP condition. Figure 5 shows that A with 120 seconds of primary-EP (A_2) and B with 60 seconds (B_1) had similar initial surface roughness. The martensite fractions of A_2 and B_1 with different

Table II. Material Parameters for EP Simulation

Parameter	Name	Units	Value	References
Diffusion Coefficient of Fe^{2+}	D_{Fe2+}	$m^2\ s^{-1}$	7.2×10^{-10}	[28]
Diffusion Coefficient of Fe^{3+}	D_{Fe3+}	$m^2\ s^{-1}$	6.1×10^{-10}	[28]
Diffusion Coefficient of H^+	D_{H+}	$m^2\ s^{-1}$	9.312×10^{-9}	[28]
Diffusion Coefficient of Cl^-	D_{Cl-}	$m^2\ s^{-1}$	2.032×10^{-9}	[28]
Reference Exchange Current Density	i_0	$A\ m^{-2}$	15.4	[29]
Charge Transfer Coefficient	α	—	0.5	[28]
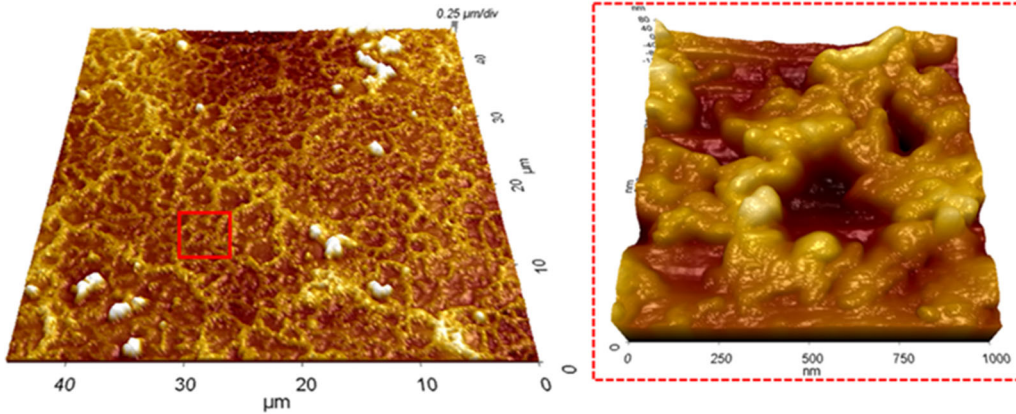
Fig. 4—Atomic force microscope images to observe the morphological characteristics of surface asperity: the 3D image obtained for 45×45 μm^2 region, and 1×1 μm^2 region for 30 seconds primary-EP treated specimen A.
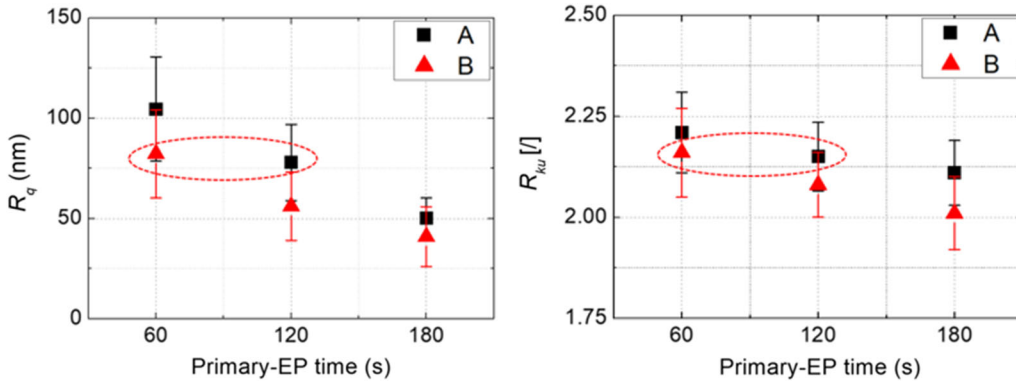
Fig. 5—Changes in surface roughness parameter for specimens A and B over primary-EP duration (60, 120, and 180 seconds): R_q values, and R_{ku} values.

austenite stability but similar surface morphologies are shown in Figure 6(c). After 30 seconds of the secondary-EP treatment, the martensite fractions of specimens A_2 and B_1 were 24.9, and 19.2 pct, respectively. To investigate the martensitic transformation behavior caused by the difference in austenite stability between specimens A_2 and B_1 specimens, the critical energy required for martensitic transformation (U^c) was calculated. The critical martensitic transformation energy is the threshold energy required to induce the austenite-martensite transformation at room temperature (25 °C), and it is equivalent to the difference in free-energy between austenite and martensite at the M_s temperature and at room temperature ($\Delta G_{M_s}^{\gamma \rightarrow \alpha'} - \Delta G_{25°C}^{\gamma \rightarrow \alpha'}$). This implies that if an energy equivalent to the critical martensitic transformation is provided, an austenite-martensite phase transformation can occur at room temperature. In this study, the energy source considered was the mechanical stress induced by charge build-up. The free-energy curves for austenite and martensite in specimens A_2 and B_1 were obtained using Thermo-Calc[32] as a function of temperature [Figure 9(a)]. The M_s temperatures for specimens A_2 and B_1 were calculated as -87 °C and -81 °C, respectively, according to the following equation[33]:
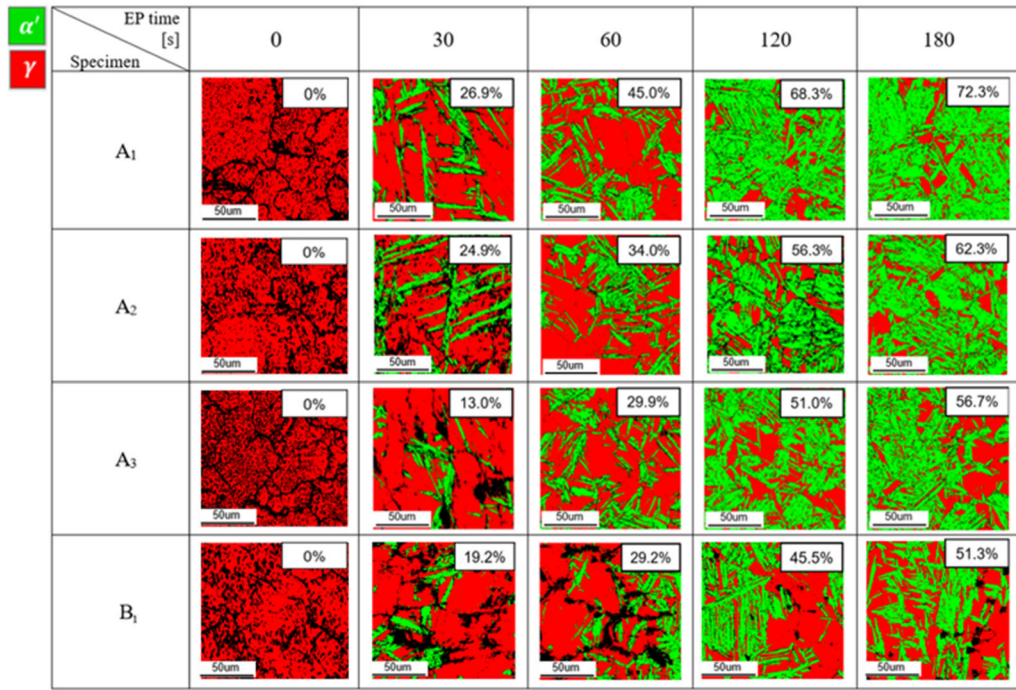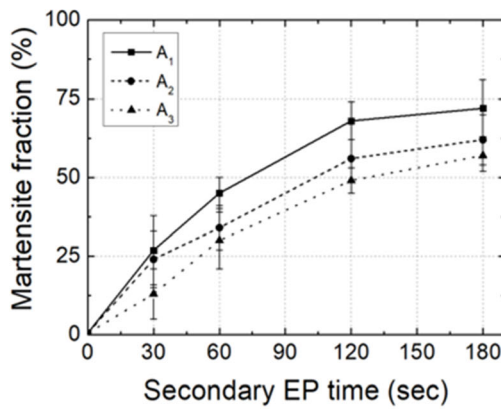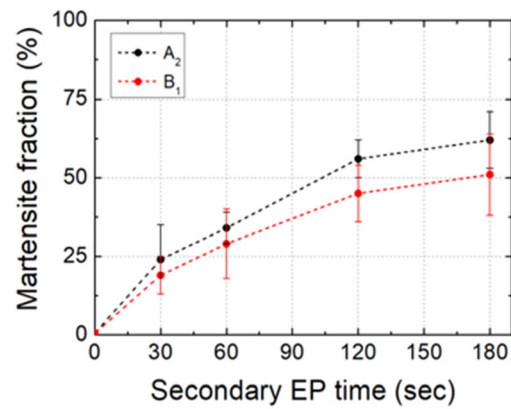
Fig. 6—(*a*) Phase map obtained from EBSD measurements of specimens with various initial surface roughness and different compositions treated by secondary-EP for duration of 30, 60, 120, and 180 seconds, and martensite fraction obtained from EBSD measurements of specimens with (*b*) various initial surface roughness and (*c*) austenite stability.
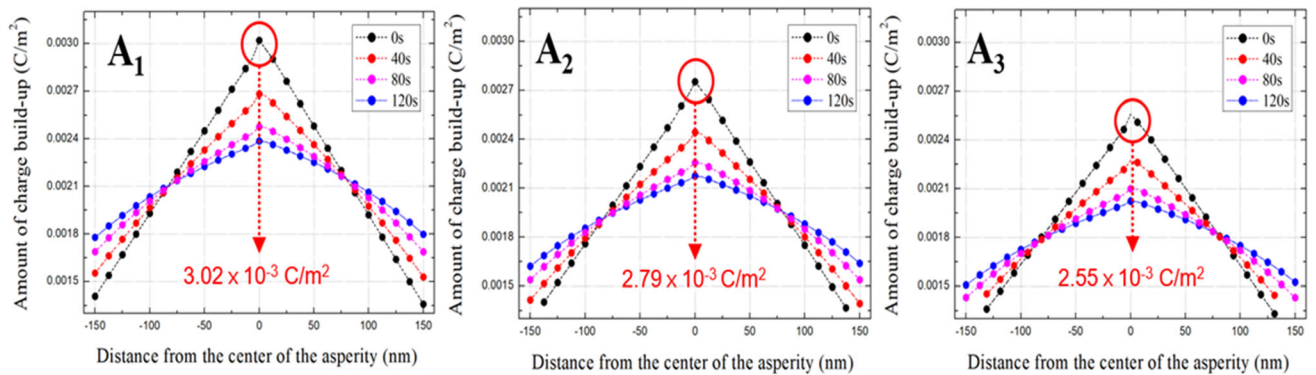

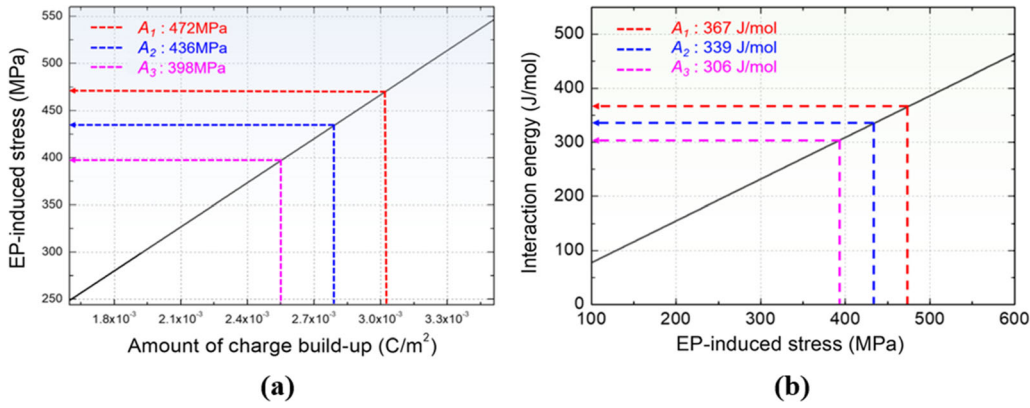Fig. 7—Maximum amount of charge build-up under application of 20 V for the asperity of specimen A_1, A_2, and A_3.

Fig. 8—(*a*) EP-induced stress caused by the amount of charge build-up obtained by DFT calculation; depending on the initial surface roughness, the degree of charge build-up-induced stress varies, and (*b*) Interaction energy accompanying the lattice deformation during martensitic transformation induced by EP-induced stress.
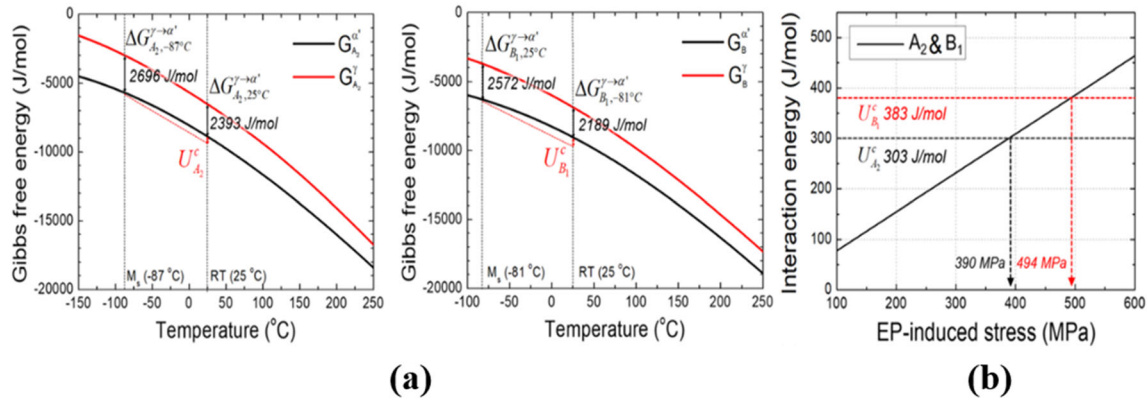
Fig. 9—(*a*) Temperature-dependent Gibbs free energy change of martensite and austenite at room temperature (25 °C) and M_s temperature (− 87 °C and − 81 °C) calculated by Thermo-Calc for specimen A$_2$ and B$_1$ respectively, (*b*) Interaction energy induced by EP-induced stress; almost identical interaction energy data were obtained for both specimens A$_2$ and B$_1$.

$$M_s(°C) : 499 - 308C - 32.4Mn - 27Cr - 16.2Ni \\ - 10.8Si - 10.8Mo - 10.8W \text{ [wt pct]} \quad [8]$$

Using the obtained M_s temperatures, the critical martensitic transformation energies for A$_2$ and B$_1$ alloys were calculated as follows:

$$U_{A_2}^c(-87°C) : \Delta G_{A,-87°C}^{\gamma \to \alpha'} - \Delta G_{A,25°C}^{\gamma \to \alpha'} = 2696 - 2393 \\ = 303(J/mol) \quad [9]$$

$$U_{B_1}^c(-81°C) : \Delta G_{B_1,-81°C}^{\gamma \to \alpha'} - \Delta G_{B_1,25°C}^{\gamma \to \alpha'} = 2572 - 2189 \\ = 383(J/mol) \quad [10]$$

The critical martensitic transformation energy for A$_2$ is 80 J/mol lower than that for B$_1$, which means that martensitic transformation can occur in A$_2$ even with a smaller transformation driving force. As shown in Figure 9(b), the martensitic transformation in A$_2$ occurs when the charge build-up-induced stress exceeds

390 MPa, which is higher than the critical martensitic transformation energy (303 J/mol). For B$_1$, the martensitic transformation requires a charge build-up–induced stress of at least 494 MPa, which exceeds the critical martensitic transformation energy (383 J/mol). These findings explain the higher martensite fraction observed in A$_2$ than that in B$_1$, as observed in the EBSD analysis results [Figure 6(c)].

Meanwhile, despite A$_2$ having a lower M_s temperature than B$_2$, martensitic transformation occurs more prevalently in A$_2$ than in B$_1$, resulting in opposite outcomes for thermal and mechanical stability. This phenomenon has been observed in other metallic materials,[34] and it is because the stress-induced martensitic transformation tendency is predominantly determined by the stacking fault energy (SFE). To compare the relative mechanical stability of A$_2$ and B$_1$ specimens, the SFE was calculated with the following empirical equation.[35]

$$\gamma_{SF}(mJ/m^2) = 16.7 + 2.1Ni - 0.9Cr + 26C \text{[wt pct]} \quad [11]$$

The SFEs of A$_2$ and B$_1$ were calculated to be 16.7 and 17.3 mJ/m^2, respectively. This means that A$_2$ has a lower SFE than B$_1$ and is more prone to the formation

of stacking faults, indicating an increased tendency for martensitic transformation.

V. CONCLUSION

Herein, the martensitic transformation in various metastable austenitic stainless steels with different surface roughness and austenite stabilities is examined using the EP-induced martensitic transformation theory. When the initial surface roughness of R_q and R_{ku} is low owing to a longer primary-EP treatment duration, the amount of charge build-up on the specimen's free surface decreases, reducing the driving force for stress-induced martensitic transformation. Additionally, by calculating the critical energy required for martensitic transformation, we found that even under lower stress-induced martensitic transformation driving forces, the low austenite stability specimens underwent transformation compared with the high austenite stability specimens. These results provided strong evidence proving the existence of the intrinsic effect of current, which is represented by the stress generation effect due to charge build-up similar to the athermal effect.

CONFLICT OF INTEREST

On behalf of all authors, the corresponding author states that there is no conflict of interest.

OPEN ACCESS

REFERENCES

1. O. Troitskii: *ZhETF Pis Ma Redaktsiiu*, 1969, vol. 10, pp. 18–22.
2. H. Conrad: *Mater. Sci. Eng. A*, 2000, vol. 287, pp. 276–87.
3. K. Okazaki, M. Kagawa, and H. Conrad: *Mater. Sci. Eng.*, 1980, vol. 45, pp. 109–16.
4. C. Ross and J.T. Roth: *ASME Int. Mech. Eng. Congr. Expos.*, 2005, vol. 42347, pp. 363–72.
5. C.D. Ross, D.B. Irvin, and J.T. Roth: *J. Eng. Mater. Technol.*, 2007, vol. 129, pp. 342–47.
6. W.A. Salandro, J.J. Jones, T.A. McNeal, J.T. Roth, S.-T. Hong, and M.T. Smith: *J. Manuf. Sci. Eng.*, 2010, vol. 132, pp. 13–32.
7. M.-J. Kim, K. Lee, K.H. Oh, I.-S. Choi, H.-H. Yu, S.-T. Hong, and H.N. Han: *Scripta Mater.*, 2014, vol. 75, pp. 58–61.
8. A. Ghiotti, S. Bruschi, E. Simonetto, C. Gennari, I. Calliari, and P. Bariani: *CIRP Ann.*, 2018, vol. 67, pp. 289–92.
9. M. Li, D. Guo, J. Li, S. Zhu, C. Xu, K. Li, Y. Zhao, B. Wei, Q. Zhang, and X. Zhang: *Mater. Sci. Eng. A*, 2018, vol. 722, pp. 93–98.
10. P.S. McNeff and B.K. Paul: *J. Alloys Compd.*, 2020, vol. 829, p. 154438.
11. J. Zhang, L. Zhan, and S. Jia: *Adv. Mater. Sci. Eng.*, 2014, vol. 2014, p. 240879.
12. W. Wang, R. Li, C. Zou, Z. Chen, W. Wen, T. Wang, and G. Yin: *Mater. Des.*, 2016, vol. 92, pp. 135–42.
13. H.-J. Jeong, M.-J. Kim, J.-W. Park, C.D. Yim, J.J. Kim, O.D. Kwon, P.P. Madakashira, and H.N. Han: *Mater. Sci. Eng. A*, 2017, vol. 684, pp. 668–76.
14. Y.S. Zheng, G.Y. Tang, J. Kuang, and X.P. Zheng: *J. Alloys Compd.*, 2014, vol. 615, pp. 849–53.
15. K. Jeong, S.-W. Jin, S.-G. Kang, J.-W. Park, H.-J. Jeong, S.-T. Hong, S.H. Cho, M.-J. Kim, and H.N. Han: *Acta Mater.*, 2022, vol. 232, p. 117925.
16. H.-J. Jeong, M.-J. Kim, S.-J. Choi, J.-W. Park, H. Choi, V.T. Luu, S.-T. Hong, and H.N. Han: *Appl. Mater. Today*, 2020, vol. 20, p. 100755.
17. Z. Tang, H. Du, K. Tao, J. Chen, and J. Zhang: *J. Mater. Process. Technol.*, 2019, vol. 263, pp. 343–55.
18. M.-J. Kim, S. Yoon, S. Park, H.-J. Jeong, J.-W. Park, K. Kim, J. Jo, T. Heo, S.-T. Hong, S.H. Cho, Y. Kwon, I. Choi, M. Kim, and H.N. Han: *Appl. Mater. Today*, 2020, vol. 21, p. 100874.
19. G. Yang, B. Wang, K. Tawfiq, H. Wei, S. Zhou, and G. Chen: *Surf. Eng.*, 2017, vol. 33, pp. 149–66.
20. P. Bała, M. Gajewska, G. Cios, J. Kawałko, M. Wątroba, W. Bednarczyk, and R. Dziurka: *Mater. Charact.*, 2022, vol. 186, p. 111766.
21. H. Gwon, J. Chae, C. Jeong, H. Lee, D.H. Kim, S.Y. Anaman, D. Jeong, H.-H. Cho, Y.-K. Kwon, S.-J. Kim, and H.N. Han: *Acta Mater.*, 2023, vol. 245, p. 118612.
22. Q. Yang, L. Qiao, S. Chiovelli, and J. Luo: *Scripta Mater.*, 1999, vol. 40, pp. 1209–14.
23. A.Y. Adesina, M. Hussain, A.S. Hakeem, A.S. Mohammed, M.A. Ehsan, and A. Sorour: *Met. Mater. Int.*, 2022, vol. 28, pp. 1–7.
24. E.S. Gadelmawla, M.M. Koura, T.M.A. Maksoud, I.M. Elewa, and H.H. Soliman: *J. Mater. Process. Technol.*, 2022, vol. 123, pp. 133–45.
25. Electrodeposition Module User's Guide, COMSOL Multiphysics® v. 6.1. COMSOL AB, Stockholm, Sweden. 2022.

26. C. Schotten, T.P. Nicholls, R.A. Bourne, N. Kapur, B.N. Nguyen, and C.E. Willans: *Green Chem.*, 2020, vol. 22, pp. 3358–75.
27. A.J. Bard, L.R. Faulkner, and H.S. White: *Electrochemical Methods: Fundamentals and Applications*, 2nd ed. Wiley, New Jersey, 2022.
28. X. You, Q. Ye, and P. Cheng: *J. Electrochem. Soc.*, 2017, vol. 164, p. E3386.
29. L. Cifuentes and J. Simpson: *Chem. Eng. Sci.*, 2005, vol. 60, pp. 4915–23.
30. H.N. Han, C.G. Lee, C.-S. Oh, T.-H. Lee, and S.-J. Kim: *Acta Mater.*, 2004, vol. 52, pp. 5203–14.
31. M.S. Wechsler: *Trans. AIME*, 1953, vol. 197, pp. 1503–15.
32. J.-O. Andersson, T. Helander, L. Höglund, P. Shi, and B. Sundman: *Calphad*, 2002, vol. 26, pp. 273–312.
33. P. Payson: *Trans. Am. Soc. Met.*, 1944, vol. 33, pp. 261–80.
34. H.-S. Noh, J.-H. Kang, K.-M. Kim, and S.-J. Kim: *Mater. Trans. A*, 2019, vol. 50A, pp. 616–24.
35. P.J. Brofman and G.S. Ansell: *Mater. Trans. A*, 1978, vol. 9A, pp. 879–80.